


Article

ADP-Induced Conformational Transition of Human Adenylate Kinase 1 Is Triggered by Suppressing Internal Motion of $\alpha_3\alpha_4$ and $\alpha_7\alpha_8$ Fragments on the ps-ns Timescale

Chenyun Guo ^{1,†}, Haoran Zhang ^{2,†} , Weiliang Lin ¹, Hanyu Chen ¹, Ting Chang ¹, Zhihua Wu ¹, Jiaxin Yu ¹ and Donghai Lin ^{1,*}

¹ Key Laboratory of Chemical Biology of Fujian Province, College of Chemistry and Chemical Engineering, Xiamen University, Xiamen 361005, China; guochy78@xmu.edu.cn (C.G.); 20520181152581@stu.xmu.edu.cn (W.L.); xmtonychen@163.com (H.C.); ctingmelody@163.com (T.C.); wuzh@xmu.edu.cn (Z.W.); yujiixin2017@126.com (J.Y.)

² Department of Pathogenic Biology, School of Basic Medicine, Tongji Medical College, Huazhong University of Science and Technology, Wuhan 430030, China; hrzhang@outlook.com

* Correspondence: dhl@xmu.edu.cn

† These authors contributed equally to this work.

Abstract: Human adenylate kinase 1 (*hAK1*) plays a vital role in the energetic and metabolic regulation of cell life, and impaired functions of *hAK1* are closely associated with many diseases. In the presence of Mg^{2+} ions, *hAK1* in vivo can catalyze two ADP molecules into one ATP and one AMP molecule, activating the downstream AMP signaling. The ADP-binding also initiates AK1 transition from an open conformation to a closed conformation. However, how substrate binding triggers the conformational transition of *hAK1* is still unclear, and the underlying molecular mechanisms remain elusive. Herein, we determined the solution structure of apo-*hAK1* and its key residues for catalyzing ADP, and characterized backbone dynamics characteristics of apo-*hAK1* and *hAK1*- Mg^{2+} -ADP complex (holo-*hAK1*) using NMR relaxation experiments. We found that ADP was primarily bound to a cavity surrounded by the LID, NMP, and CORE domains of *hAK1*, and identified several critical residues for *hAK1* catalyzing ADP including G16, G18, G20, G22, T39, G40, R44, V67, D93, G94, D140, and D141. Furthermore, we found that apo-*hAK1* adopts an open conformation with significant ps-ns internal mobility, and Mg^{2+} -ADP binding triggered conformational transition of *hAK1* by suppressing the ps-ns internal motions of $\alpha_3\alpha_4$ in the NMP domain and $\alpha_7\alpha_8$ in the LID domain. Both $\alpha_3\alpha_4$ and $\alpha_7\alpha_8$ fragments became more rigid so as to fix the substrate, while the catalyzing center of *hAK1* experiences promoted μ s-ms conformational exchange, potentially facilitating catalysis reaction and conformational transition. Our results provide the structural basis of *hAK1* catalyzing ADP into ATP and AMP, and disclose the driving force that triggers the conformational transition of *hAK1*, which will deepen understanding of the molecular mechanisms of *hAK1* functions.

Keywords: *hAK1*; backbone dynamics; enzymatic activity; solution structure



Citation: Guo, C.; Zhang, H.; Lin, W.; Chen, H.; Chang, T.; Wu, Z.; Yu, J.; Lin, D. ADP-Induced Conformational Transition of Human Adenylate Kinase 1 Is Triggered by Suppressing Internal Motion of $\alpha_3\alpha_4$ and $\alpha_7\alpha_8$ Fragments on the ps-ns Timescale. *Biomolecules* **2022**, *12*, 671. <https://doi.org/10.3390/biom12050671>

Academic Editor: Jose R. Bayascas

Received: 12 April 2022

Accepted: 3 May 2022

Published: 6 May 2022

Publisher's Note: MDPI stays neutral with regard to jurisdictional claims in published maps and institutional affiliations.



Copyright: © 2022 by the authors. Licensee MDPI, Basel, Switzerland. This article is an open access article distributed under the terms and conditions of the Creative Commons Attribution (CC BY) license (<https://creativecommons.org/licenses/by/4.0/>).

1. Introduction

Adenylate kinases (AKs) can read cellular adenine nucleotide balance and generate AMP molecules to trigger AMP signaling. Together with downstream AMP signaling (AK→AMP→AMP-sensors), AKs play fundamental roles in cell differentiation, cell polarity maintenance, and cell division [1–4]. As the crucial metabolic monitor of AMP signaling, the AKs family consists of nine major isoforms (AK1–AK9). AK1 is the major AMP generator and participates in many physiological processes [5,6]. The determined *E. coli* AK1 three-dimensional structure consists of LID, NMP, and CORE domains, and the LID and NMP domains are responsible for binding substrates, while the CORE domain governs the overall stability of the enzyme [7]. Furthermore, the CORE and NMP domains are

conserved in different species whereas the LID domain is quite different. In the presence of Mg^{2+} , AK1 can catalyze ATP and AMP into ADP. Due to ATP and AMP instabilities, analogs of ATP and AMP (AP_4A , AP_5A , AP_6A) have been extensively used to exploit the interactions between AK1 and its substrates ATP and AMP [8]. The comparison of the crystal structures of *E.coli* AK1 in free form (PDB ID: 4AKE) and in complex with AP_5A (PDB ID: 1AKE) displays that AK1 undergoes significant conformational change as both LID and NMP domains get close to the CORE domain when AK1 exerts its catalytic function [9,10]. Moreover, Pelz et al. demonstrate that AK1 binds ATP and AMP with an induced-fit mechanism in which substrate binding initiates AK1 transition from an open state to a closed state [11].

On the other hand, AK1 can reversibly catalyze ADP into ATP and AMP. Filip-pakopoulos et al. have determined the complex structure of *hAK1* with the homologs of two ADP molecules, B_4P (PDB ID: 2C95). The complex structure of *hAK1*- B_4P indicates that *hAK1* also adopts a closed conformation similar to the complex structure of *hAK1*- AP_5A (PDB ID: 1Z83). The comparison of the apo-*MtbAK1* structure (PDB: 1P4S) with the *MtbAK1*- Mg^{2+} -ADP complex structure (PDB ID: 2CDN) illustrates that ADP binding also induces the conformational transition of AK1 from open to closed states [12,13]. Nevertheless, how substrate binding triggers the conformational transition of AK1 is still unclear. Herein, we determined the solution structure of *hAK1* and identified key residues in *hAK1* for catalyzing ADP by a combination of NMR chemical shift perturbation, enzyme activity assays, and point mutation experiments. Furthermore, we addressed the backbone dynamics characteristics of *hAK1* when it exerted its catalytic function with NMR relaxation experiments. Our results are beneficial to exploring the AK1 catalytic cycle and providing a further mechanistic understanding of AK1 functions.

2. Materials and Methods

2.1. Preparation of Recombinant *hAK1* and Its Mutants

Genes of *hAK1* and its variants were separately cloned into the pGEX-6p-1 vector. Fusion proteins were expressed in *E. coli* BL21(DE3) at 22 °C and extracted by sonication, then purified by a GST affinity column. PreScission Protease was used to remove the GST tag at 4 °C. Finally, the target proteins were eluted into the NMR buffer (10 mM Na_2HPO_4 , 100 mM Na_2SO_4 , 50 mM NaCl, pH 6.2). Protein purities were analyzed by using 15% (*w/v*) SDS-PAGE. Single-point mutations were conducted through PCR and verified by DNA sequencing from the Sangon Company.

2.2. Structure Calculation

Backbone and side-chain chemical shifts of apo-*hAK1* have been assigned in our previous work (BMRB ID: 18133) [14]. 1H - 1H NOE resonances in 3D ^{13}C - and ^{15}N -edited NOESY-HSQC spectra were manually and automatically assigned by using the Aria 2.3 software [15]. Resonance integrals of the NOESY-HSQC cross-peaks were used to generate 1H - 1H distance restraints. Backbone dihedral restraints were predicted with the TALOS-N program based on assigned chemical shifts of *hAK1* [16]. Annealing parameters were optimized for the final run (20,000, 1000, 120,000, and 96,000 for high temperature, refinement, cool1, and cool2 steps). Ultimately, 300 models of *hAK1* were calculated and refined with Aria 2.3, from which 20 lowest-energy structures were chosen as the final conformational ensemble. The PROCHECK program was used to assess the structural quality of the *hAK1* protein [17].

2.3. NMR Chemical Shift Perturbation Experiments

NMR titration experiments were conducted on Bruker Avance III 600 MHz spectrometer (Bruker, Billerica, MA, USA) at 298K. The apo-*hAK1* sample was solved in NMR buffer added with 5 mM EDTA. The holo-*hAK1* sample was solved in NMR buffer added with 5 mM $MgCl_2$, and ADP was titrated step-by-step according to the following molar ratios

of protein: ligand: 1:0, 1:0.5, 1:1, 1:2, 1:3, 1:4, 1:5, 1:6, 1:7, 1:8. We calculated chemical shift perturbations ($\Delta\delta$) of *hAK1* at the molar ratio of 1:8, using the following formula:

$$\Delta\delta = \sqrt{\Delta\delta^2(^1\text{H}) + \Delta\delta^2(^{15}\text{N})}/25, \quad (1)$$

where $\Delta\delta(^1\text{H})$ is the perturbation in proton and $\Delta\delta(^{15}\text{N})$ is the perturbation in nitrogen dimension.

2.4. Enzymatic Activity Assay

Enzymatic activities of *hAK1* and its mutants were assessed in a coupling reaction with hexokinase-glucose-6-phosphate dehydrogenase, and the fluorescence intensity of final product NADPH at 456 nm was proportional to the enzymatic activity of *hAK1* [18]. In detail, the enzymatic activities were measured in a reaction solution (50 mM Tris-HCl, 7.2 mM MgCl₂, 2 mM Glucose, 1.64 mM NADP, 500 µg/L BSA, 3 mM ADP, 0.1 µg/mL *hAK1*, and 0.7 U/mL hexokinase-glucose-6-phosphate dehydrogenase) at 37 °C for 5 min. Then, a stop solution (10 mM NaOH, 5 mM EDTA) was added into the reaction solution to stop the reaction.

2.5. Backbone Relaxation Measurements

Relaxation experiments were conducted on Bruker Avance III 600 MHz spectrometer at 298 K. Standard pulse sequences were used to obtain longitudinal and transverse relaxation rates R_1 and R_2 , as well as $\{^1\text{H}\}$ - ^{15}N heteronuclear steady-state NOEs (hnNOEs). For ^{15}N T_1 measurements, the delay times were set to 0.01, 0.05, 0.1, 0.2, 0.4, 0.8, 1.2, 1.5, and 1.8 s in random order. For ^{15}N T_2 measurements, the delay times were set to 16.96, 33.92, 50.88, 67.84, 84.80, 101.76, 118.72, 135.68, 152.64, and 186.56 ms in random order. Two delay times were duplicated for both T_1 and T_2 experiments at the end of the experiments to estimate uncertainties of T_1 and T_2 values. For hnNOE experiments, a delay of 2 s was followed by ^1H saturation of 3 s, and in the control experiments without ^1H saturation, a total delay of 5 s was applied. The relaxation data were processed and analyzed with Bruker Dynamics Center 2.3 (Bruker, Billerica, MA, USA).

2.6. Model-Free Analysis

Model-free analysis of relaxation parameters R_1 , R_2 , and hnNOE was performed with the TENSOR2 and FAST-Modelfree programs following the Lipari-Szabo formalism [19–22]. Internal motions of backbone amide groups were fitted to five different model-free models described with a combination of S^2 , τ_e , and R_{ex} . S^2 is the squared order parameter, τ_e is the correlation time of the internal motion (ps-ns time scale), and R_{ex} is the chemical exchange rate (µs-ms time scale) contributing to R_2 . An axially symmetric diffusion model was chosen for the model-free calculations. The F -test statistics were used to select the model satisfying the data with the lower number of parameters.

2.7. Reduced Spectral Density Mapping

Reduced spectral density mapping was conducted on the obtained relaxation data R_1 , R_2 , and hnNOE [23]. These data were converted into three $J(\omega)$ values $J(0)$, $J(\omega_N)$, $J(0.87\omega_H)$ using the script reported by Leo Spyropoulos [24].

3. Results

3.1. NMR Solution Structure of *hAK1*

To disclose molecular mechanisms underlying *hAK1* catalyzing ADP, we determined the solution structure of *hAK1* using heteronuclear multi-dimensional NMR spectroscopy. The final structure ensemble consists of 20 lowest-energy models (Figure 1A), and the NMR restraints and structure statistics are shown in Table 1. Structural quality analysis by the PROCHECK program illustrated that most of the modeled residues were in preferred and allowed regions (Table 1). The root-mean-square deviation (RMSD) for the 20 structural

models to the mean structure reached 0.57 Å and 0.84 Å for backbone atoms and heavy atoms, respectively, indicating a well-defined structure ensemble. The solution structure of *hAK1* has been deposited in the Protein Data Bank with an accession code of 7X7S.

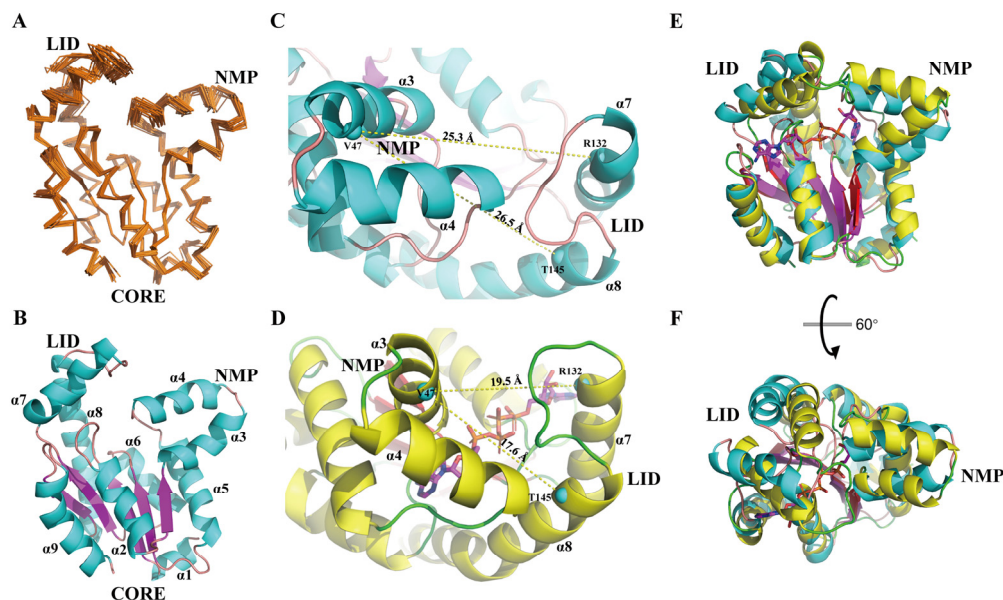


Figure 1. Standalone and comparative representation of the apo-*hAK1* structure. (A) Superposition of 20 lowest-energy structures of apo-*hAK1* represented as ribbons (PDB ID: 7X7S). (B) Mean structure of apo-*hAK1* depicted in cartoon. α -helices and β -strands are colored in cyan and purple, respectively. (C) Conformation of NMP and LID domains in apo-*hAK1*. (D) Conformation of NMP and LID domains in the *hAK1*-B₄P complex (PDB ID: 2C95). The C α atoms of V47 in α_3 , R132 in α_7 and T145 in α_8 are selected to optimally exhibit the distances between α_3 and α_7 or α_8 , which are displayed as cyan spheres. The α -helices of apo-*hAK1* and B₄P-complexed *hAK1* are colored in cyan and yellow, respectively. (E,F) Superposition of 7X7S (α -helices in cyan and β -strands in purple) and 2C95 (α -helices in yellow and β -strands in red) structures. 7X7S atom coordinates were RMS fitted to 2C95 by C α atoms in α_1 , α_2 , α_5 , α_6 , α_9 , and β_1 - β_5 for visualization.

Overall, *hAK1* adopted a globular fold comprising 9 α -helices (α_1 : 2–7, α_2 : 21–32, α_3 : 39–49, α_4 : 52–63, α_5 : 69–83, α_6 : 99–109, α_7 : 122–135, α_8 : 143–167, α_9 : 179–193) and a five-stranded β -sheet (β_1 : 9–14, β_2 : 35–38, β_3 : 89–83, β_4 : 114–119, β_5 : 170–174) (Figure 1B). Three domains, namely NMP, LID, and CORE were identified in the *hAK1* protein: NMP contained α_3 and α_4 ; LID consisted of α_7 and α_8 ; CORE was represented by the β -sheet surrounded by other helices. Notably, NMP and LID domains exhibited larger RMSDs than the global average due to relatively fewer NOE restraints (Figure 1A), indicative of their structural flexibilities in solution.

To investigate structural alterations of *hAK1* upon binding to its substrates, we compared the three-dimensional structures of apo-*hAK1* (PDB ID: 7X7S) and *hAK1*-B₄P complex (PDB ID: 2C95). Expectedly, NMP and LID domains exhibited noticeable conformational changes. The NMP and LID domains adopted an open conformation in apo-form, characterized by a relatively large distance between α_3 and α_7 or α_8 of 25.3 Å or 26.5 Å, respectively (Figure 1C). Upon B₄P binding to *hAK1*, both NMP and LID domains moved inward, resulting in reduced corresponding distances of 19.5 Å or 17.6 Å, respectively (Figure 1D). Furthermore, the local structural alignment of apo-*hAK1* with B₄P-complexed *hAK1* gave an RMSD of 1.73 Å for the CORE domain, 5.17 Å for the region consisting of NMP and LID domains (Figure 1E–F). Consequently, B₄P binding to *hAK1* led to a “closed” conformation for the NMP and LID domains.

Table 1. NMR restraints and structural statistics for *hAK1*.

NMR Distance and Dihedral Constraints	Values
Total unambiguous distance restraints	2603
Intra-residual	884
Sequential ($ i-j = 1$)	728
Short-range ($2 \leq i-j \leq 3$)	388
Medium-range ($4 \leq i-j \leq 5$)	144
Long-range ($ i-j > 5$)	459
Total ambiguous distance restraints	402
Total dihedral angle restraints	350
φ (backbone dihedral angle $C_{i-1}-N_i-C_{i,\alpha}-C_i$)	175
ψ (backbone dihedral angle $N_i-C_{i,\alpha}-C_i-N_{i+1}$)	175
Structural statistics	
Mean restraint violations	
Distance restraint violations ($>0.5 \text{ \AA}$)	0.90
Dihedral restraint violations ($>5^\circ$)	1.35
Average RMSD (\AA) to mean structure (all residues)	
Backbone RMSD	0.57 ± 0.09
Heavy atoms RMSD	0.84 ± 0.06
Ramachandran plot statistics ¹	
Residues in favored regions	$89.2\% \pm 1.5\%$
Residues in allowed regions	$10.6\% \pm 1.7\%$
Residues in generously allowed regions	$0.2\% \pm 0.3\%$
Residues in disallowed regions	$0\% \pm 0\%$

¹ Analyzed with PROCHECK.

3.2. Key Residues for *hAK1* Catalyzing ADP

As reported previously, *hAK1* can efficiently catalyze mutual transformation among ADP, ATP, and AMP only in the presence of some divalent ions such as Mg^{2+} [25]. To identify key residues for *hAK1* catalyzing ADP, we performed NMR titration experiments on ^{15}N -labeled *hAK1* with increasing ADP concentration in the presence of Mg^{2+} . It was previously reported that *hAK1* is associated with five statuses during its catalytic cycle: open, partially open, intermediate, partially closed, and closed [26]. Expectedly, ADP titration resulted in greater conformational exchange for *hAK1*. About 50% of peaks in the 2D 1H - ^{15}N HSQC spectra of *hAK1*/ Mg^{2+} -ADP were appreciably perturbed, including 36 vanished peaks, 40 broadened peaks and 21 shifted peaks (Figure 2A–C). These perturbed residues were identified and mapped into the three domains of apo-*hAK1* based on the backbone assignments we previously completed [14], suggesting that Mg^{2+} -ADP caused a significant change to the whole structure of apo-*hAK1* (Figure 2D). In order to identify key residues for *hAK1* catalyzing ADP, we mutated 14 significantly perturbed residues, which were situated on the *hAK1*- B_4P interface identified from the 3D structure of *hAK1* complexed with B_4P (PDB ID: 2C95), including G16, G18, G20, G22, T39, G40, R44, Q65, V67, D93, G94, R132, D140, and D141. Besides, we also mutated significantly perturbed residues V13 and V29, which were located far away from the binding interface.

The enzymatic activities of 12 *hAK1* mutants have decreased. As shown in Figure 2E, five mutations (G40A, R44A, D93A, D140A, and D141A) remarkably decreased enzymatic activities of *hAK1* by more than 90%. Moreover, four mutations (G16A, G20A, G22A, and G94A) significantly decreased enzymatic activities of *hAK1* by more than 50%. Furthermore, three mutations (G18A, T39A, and V67A) reduced enzymatic activities of *hAK1* by 20%–40%. Thus, we identified 12 key residues for *hAK1* catalyzing ADP, including G16, G18, G20, G22, T39, G40, R44, V67, D93, G94, D140, and D141, which are highlighted in the 3D structure of the *hAK1*- B_4P complex (Figure 2F). Notably, V13A and V29A mutations did not significantly decrease the enzymatic activity of *hAK1*, implying that their chemical shift perturbation was primarily caused by the overall conformational change of *hAK1* upon addition of ADP.

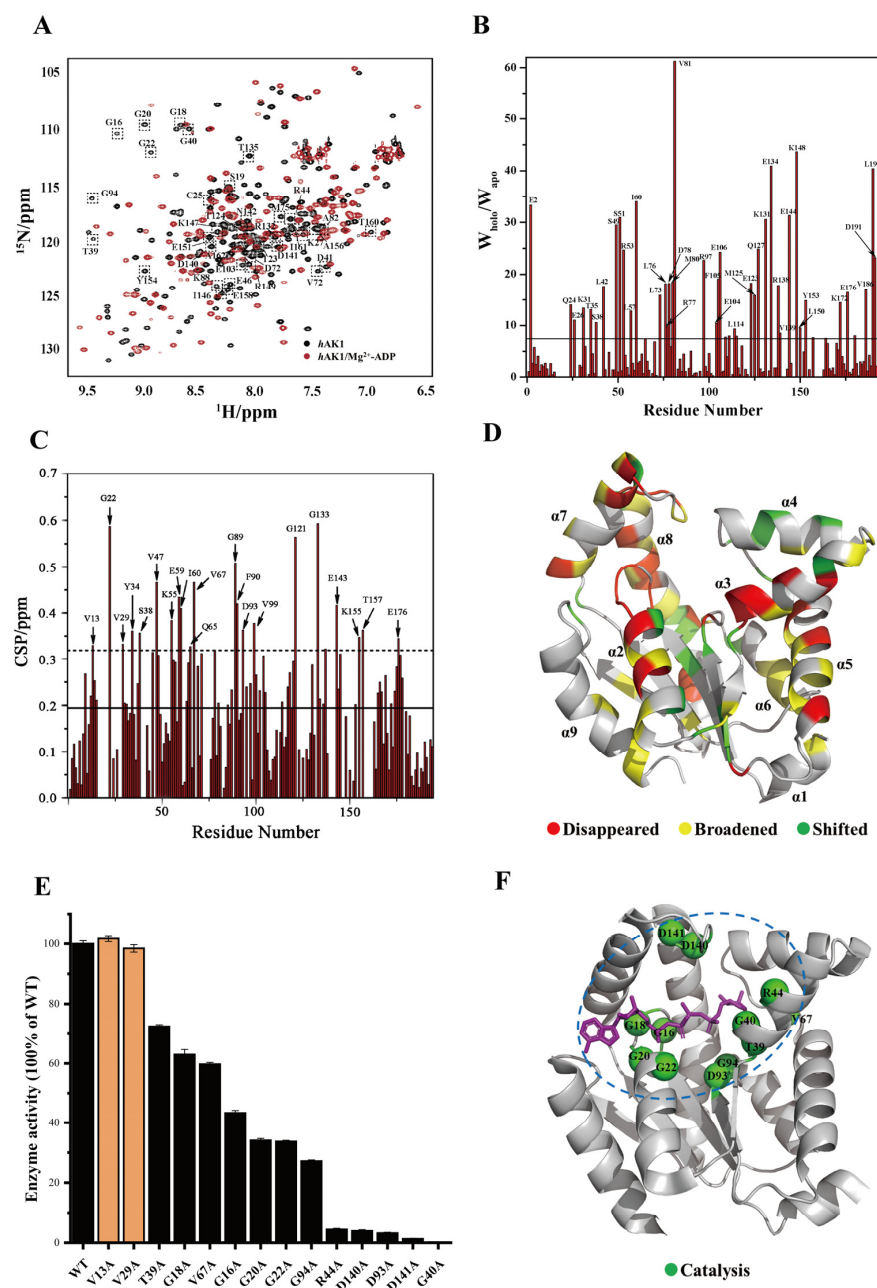


Figure 2. Determination of key residues for *hAK1* catalyzing ADP. (A) Overlaid 2D ^1H - ^{15}N HSQC spectra of the *hAK1* protein with and without Mg^{2+} -ADP addition. Black: *hAK1*, Red: *hAK1*- Mg^{2+} -ADP; dashed box represents disappeared peaks after Mg^{2+} -ADP addition. (B) Identification of residues with significant peak broadening after Mg^{2+} -ADP addition. (C) Identification of residues with significant peak shifting after Mg^{2+} -ADP addition. (D) Mapping perturbed residues onto the three-dimensional structure of apo-*hAK1* (PDB ID: 7X7S). (E) Enzymatic activity comparison of *hAK1* and its variants. (F) Mapping key residues for *hAK1* catalyzing ADP onto the 3D structure of the *hAK1*- B_4P complex (PDB ID: 2C95). Blue dashed circle: ADP catalyzing center.

3.3. Comparison of Relaxation Data between apo-*hAK1* and holo-*hAK1*

As it is known, dramatic conformational changes occurred during the *hAK1* catalytic cycle. Although structural studies have provided ample evidence for conformational changes of *hAK1*, few systematic experimental studies were reported to explore dynamic properties of the *hAK1* enzyme through its catalytic cycles [27,28]. To disclose the driving force in the conformational transition of *hAK1*, we determined backbone dynamics param-

ters of apo-*hAK1* and holo-*hAK1* (*hAK1*-Mg²⁺-ADP), including ¹⁵N longitudinal relaxation rates (R_1), ¹⁵N transverse relaxation rates (R_2) and {¹H}-¹⁵N heteronuclear steady-state NOEs (hnNOE).

The mean R_1 and R_2 values of apo-*hAK1* were $0.983 \pm 0.007 \text{ s}^{-1}$ and $16.941 \pm 0.178 \text{ s}^{-1}$, respectively (Figure 3A). After Mg²⁺-ADP addition, the mean R_1 and R_2 values became $0.917 \pm 0.041 \text{ s}^{-1}$ and $16.709 \pm 0.329 \text{ s}^{-1}$, respectively. Overall, Mg²⁺-ADP binding did not result in significant changes in mean relaxation rates for *hAK1* (Figure 3A–B). However, holo-*hAK1* displayed greater local fluctuations of the backbone relaxation parameters compared to apo-*hAK1*, especially in the $\alpha_3\alpha_4$ fragment (residues 39–72) of the NMP domain and the $\alpha_7\alpha_8$ fragment (residues 120–152) of the LID domain. Both $\alpha_3\alpha_4$ and $\alpha_7\alpha_8$ fragments of apo-*hAK1* exhibited higher R_1 values and lower R_2 values than the average values, implying that these regions might undergo significant internal motions on the ps-ns time scale with observable structural flexibility. Differently, holo-*hAK1* showed relatively stable R_1 and R_2 values across the amino acid sequence with insignificant ps-ns internal motions in $\alpha_3\alpha_4$ and $\alpha_7\alpha_8$ fragments. Besides, $\alpha_7\alpha_8$ of holo-*hAK1* displayed profoundly increased {¹H}-¹⁵N NOE values, suggesting that the LID domain became more rigid upon Mg²⁺-ADP binding. Therefore, we speculate that Mg²⁺-ADP binding remarkably changed the dynamics properties of *hAK1* by suppressing the ps-ns internal motions of $\alpha_3\alpha_4$ and $\alpha_7\alpha_8$.

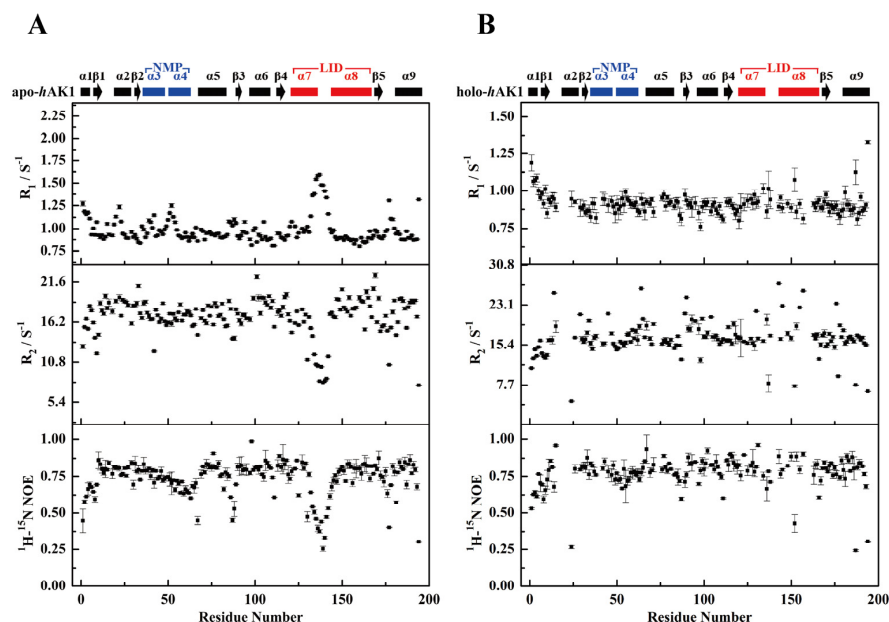


Figure 3. R_1 , R_2 , and hnNOE values of apo-*hAK1* (A) and holo-*hAK1* (B). The secondary structure elements of *hAK1* are displayed on the top of the figure. The $\alpha_3\alpha_4$ in the NMP domain and $\alpha_7\alpha_8$ in the LID domain are highlighted in blue and red, respectively.

3.4. Model-Free Analysis

The relaxation data of R_1 , R_2 , and {¹H}-¹⁵N NOE were further processed by using model-free analysis. We firstly obtained rotational diffusion tensors describing the overall tumbling of apo-*hAK1* and holo-*hAK1*. The best-fit χ^2 value of the axially symmetric diffusion model was 291.2 for apo-*hAK1* and 317.3 for holo-*hAK1*, indicative of well-fitted models. The estimated rotational correlation time (τ_m) was $13.929 \times 10^{-9} \text{ s}$ for apo-*hAK1* and $13.406 \times 10^{-9} \text{ s}$ for holo-*hAK1*. The diffusion tensor ratio $D_{//}/D_{\perp}$ was 1.190 for apo-*hAK1* and 1.149 for holo-*hAK1*, indicating that internal motions of both apo-*hAK1* and holo-*hAK1* could be described by using slightly prolate diffusion models.

The model-free analysis of relaxation data provided an internal correlation time (τ_e), and an order parameter (S^2) as well as a conformational exchange rate (R_{ex}) for describing backbone dynamics characteristic of each residue for the protein. Results derived from the model-free analysis of apo-*hAK1* showed that residues with smaller S^2 and larger

τ_e values were primarily distributed in the $\alpha_3\alpha_4$ and $\alpha_7\alpha_8$ fragments, indicating that these two fragments had apparent fast internal mobility on the ps-ns timescale (Figure 4A). However, once Mg^{2+} -ADP binding, these prominent ps-ns internal motions were attenuated, even quenched in the $\alpha_3\alpha_4$ and $\alpha_7\alpha_8$ as shown by increased S^2 and decreased τ_e values (Figure 4B). On the other hand, backbone amide groups of apo-*hAK1* did not show significant slow internal motions on the μs -ms timescale, as indicated by only one residue exhibiting an observable R_{ex} value (Figure 4C). The Mg^{2+} -ADP binding brought significant μs -ms internal motion in holo-*hAK1*, as reflected by 24 residues with large R_{ex} values, which surrounded the catalyzing center including V14, G15, V29, S45, G64, Q65, T71, G89, F90, L91, D93, Y95, V99, E104, Q111, L114, Y117, L130, E143, T145, K155, T157, K172, and E176 (Figure 4D). Notably, the LID domain exhibited promoted conformational exchange and structural flexibility, which was potentially favorable for *hAK1* exerting its catalytic functions.

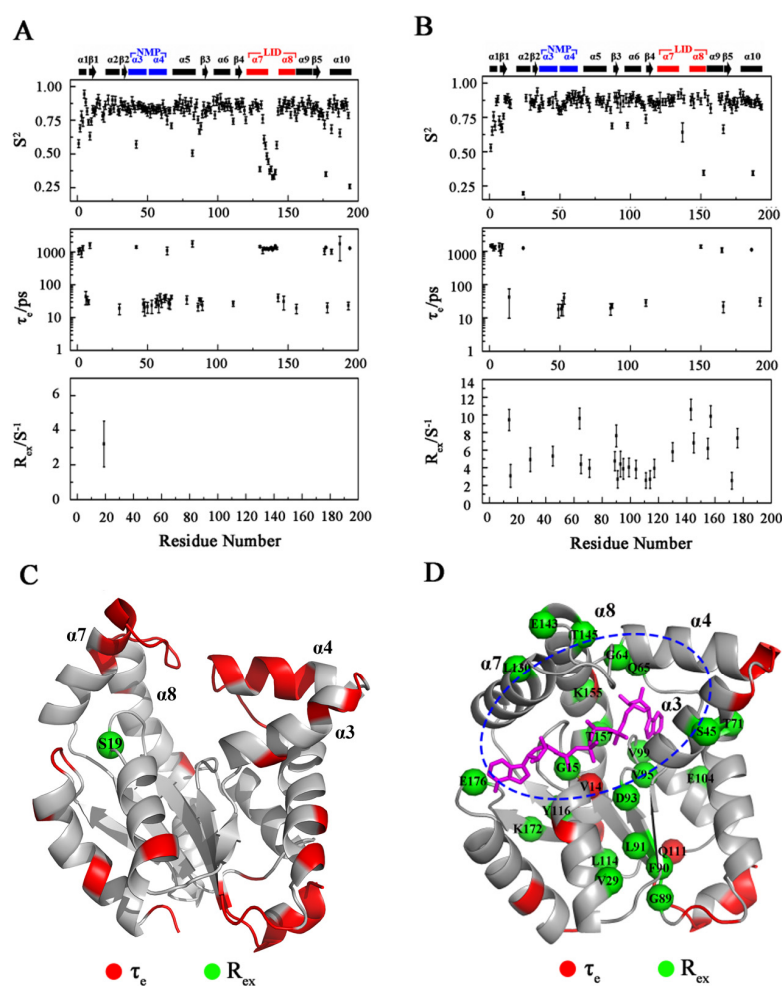


Figure 4. Model-free analyses of apo-*hAK1* and holo-*hAK1*. (A,B) Three dynamics parameters (S^2 , τ_e and R_{ex}) fitted from model-free analyses based on the obtained relaxation parameters of R_1 , R_2 , and $\{^1\text{H}\}$ - ^{15}N NOE of apo-*hAK1* (A) and holo-*hAK1* (B). (C,D) Residues with τ_e (displayed in red) and R_{ex} (shown as green balls) are mapped onto the 3D structures of apo-*hAK1* (C) and *hAK1*- Mg^{2+} - B_4P (D). Red balls: residues with τ_e and R_{ex} simultaneously. Blue dashed circle: the catalyzing center. The secondary structure elements of *hAK1* are displayed on the top of the figure. The $\alpha_3\alpha_4$ in the NMP domain and $\alpha_7\alpha_8$ in the LID domain are highlighted in blue and red, respectively.

As it is known, AK1 binds substrates in the open conformation, catalyzes the phosphotransfer reaction in the closed conformation, and releases products again in the open conformation. The holo-*hAK1* adopts a closed conformation upon Mg^{2+} -ADP binding,

which is helpful for avoiding hydrolysis of the product ATP. Note that some residues showed relatively larger S^2 values, including E26, Y34, G89, and I92 located in the CORE domain, and A120, L130, E134, S136, G137, and R138 in $\alpha_7\alpha_8$ of the NMP domain, as well as K63, G64, and V67 in $\alpha_3\alpha_4$ of the LID domain. These regions displayed relatively rigid dynamics properties, which were potentially responsible for restricting the conformational exchange required for *hAK1* binding more efficiently Mg^{2+} -ADP (Figure 5).

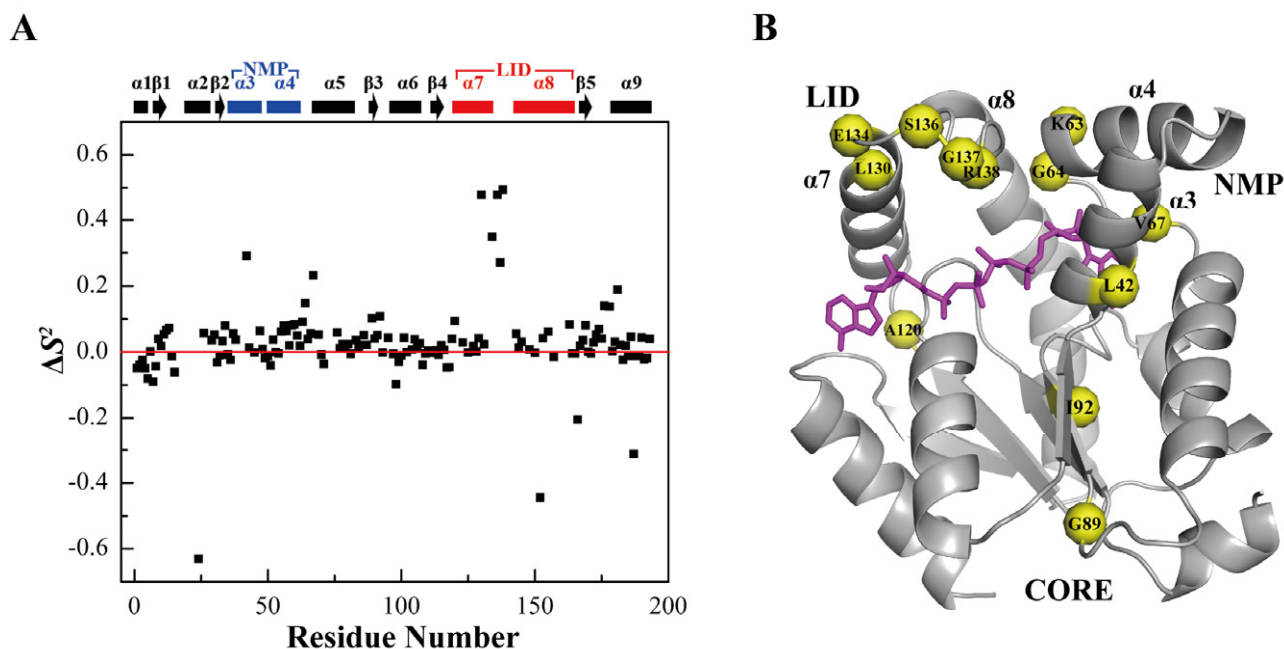


Figure 5. Comparison of the S^2 values of holo-*hAK1* with apo-*hAK1*. (A) Differences of the S^2 values between holo-*hAK1* and apo-*hAK1*. The secondary structure elements of *hAK1* are displayed on the top of the figure. The $\alpha_3\alpha_4$ in the NMP domain and $\alpha_7\alpha_8$ in the LID domain are highlighted in blue and red, respectively. (B) Residues in holo-*hAK1* with increased S^2 values are mapped onto the 3D structure of the *hAK1*- Mg^{2+} - B_4P complex.

3.5. Reduced Spectral Density Mapping

Reduced spectral density functions at three frequencies $J(0)$, $J(\omega_N)$ and $J(0.87\omega_H)$ were calculated for each residue based on the obtained ^{15}N relaxation parameters of apo-*hAK1* and holo-*hAK1*. As expected, both $\alpha_3\alpha_4$ and $\alpha_7\alpha_8$ fragments displayed different spectral density functions, similar to the above-described relaxation parameters (Figure 6).

Significantly, Mg^{2+} -ADP binding to *hAK1* increased average $J(0)$ values in the $\alpha_3\alpha_4$ and $\alpha_7\alpha_8$ fragments (Figure 7A), suggesting that both fragments had enhanced internal mobility on the μ s-ms timescale. Furthermore, Mg^{2+} -ADP binding also remarkably decreased average $J(\omega_N)$ and $J(0.87\omega_H)$ values for $\alpha_3\alpha_4$ and $\alpha_7\alpha_8$, indicative of suppressed structural flexibility on the ps-ns timescale (Figure 7B,C). It seemed that despite the overall 3D structure of holo-*hAK1* being more rigid than apo-*hAK1*, Mg^{2+} -ADP binding profoundly promoted the μ s-ms conformational exchange which potentially facilitated catalysis reaction and conformational transition. These results were basically consistent with those from the model-free analysis (Figure 4).

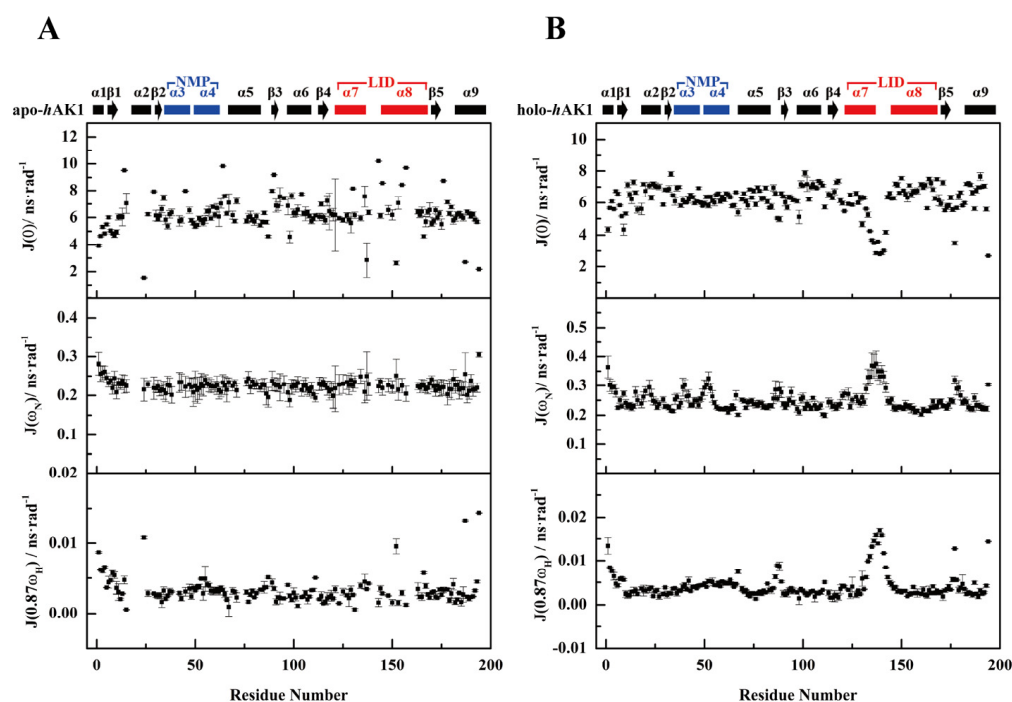


Figure 6. Spectral density functions of residues in apo-*hAK1* (A) and holo-*hAK1* (B). Analysis of reduced spectral density mapping was carried out using Mathematica notebooks from Leo Spyropoulos [24]. The secondary structure elements of *hAK1* are displayed on the top of the figure. The $\alpha_3\alpha_4$ in the NMP domain and $\alpha_7\alpha_8$ in the LID domain are highlighted in blue and red, respectively.

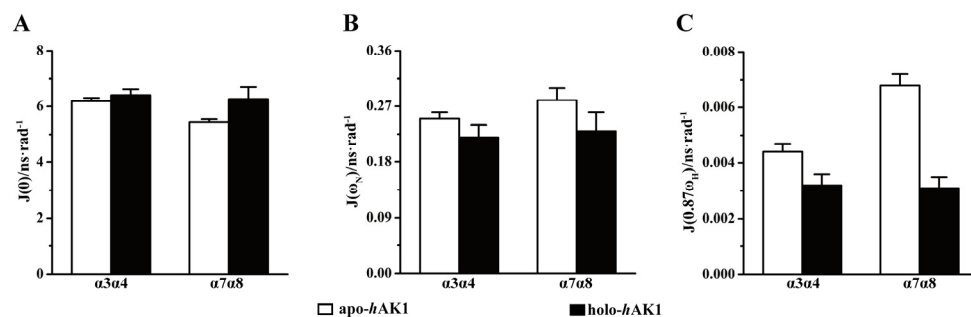


Figure 7. Comparison of spectral density functions of the $\alpha_3\alpha_4$ and $\alpha_7\alpha_8$ fragments between apo-*hAK1* and holo-*hAK1*. (A) $J(0)$; (B) $J(\omega_N)$; (C) $J(0.87\omega_H)$.

4. Discussion

We have determined the solution structure of apo-*hAK1*, and identified 12 key residues for *hAK1* catalyzing ADP, including G16, G18, G20, G22, T39, G40, R44, V67, D93, G94, D140, and D141. Both model-free analysis and spectral density analysis showed that apo-*hAK1* adopts an open conformation with significant ps-ns internal mobility, thereby allowing local structural rearrangements to accommodate *hAK1* binding Mg^{2+} and ADP. The Mg^{2+} -ADP binding substantially triggers the conformational transition of *hAK1* by suppressing the fast internal motions of $\alpha_3\alpha_4$ in the NMP domain and $\alpha_7\alpha_8$ in the LID domain, and simultaneously promoting the slow internal motions of the protein. Upon *hAK1* binding Mg^{2+} and ADP, both $\alpha_3\alpha_4$ and $\alpha_7\alpha_8$ become more rigid so as to fix the substrate, while the catalyzing center of *hAK1* experiences promoted μ s-ms conformational exchange, potentially facilitating catalysis reaction and conformational transition.

While our study suggests several potential determinants of *hAK1*'s catalyzing functionality from a view of structural biology and biophysics, certain considerations arising from our interpretation of the results need in-depth discussion. For example, because of the

inherent conformation averaging effect of the in-solution NMR sampling, the rare conformations existing at the saddle points on the free energy landscape might be omitted during structure calculation and, thus, are not necessarily present in the final NMR ensemble. Expectedly, MD simulations would be helpful to remedy the lack of atom-level portrayal of important conformations, which are calculated based on NMR-derived constraints. MD simulations can catch vital biomolecular processes by revealing atomic coordinates at fs-level resolution, and predict how protein dynamics respond to both perturbations imposed on residues and introduction of ligands [29]. Recent advances in accelerated MD might particularly enhance the sampling of biomolecular binding events on an enlarged simulation timescale than the conventional ns- μ s all-atom simulation [30]. The advanced MD simulation methodology will allow for the thorough characterization of lid motion and substrate binding thermodynamics and kinetics of *hAK1*.

Another critical question lies before this study about how the internal motion of $\alpha_3\alpha_4$ and $\alpha_7\alpha_8$ fragments on the ps-ns timescale induces the biochemically significant steps that occur on the μ s-ms timescale. Previous studies reported that the adenylate kinase from *Aquifex aeolicus* (*Aquifex* Adk) exhibits a free-energy landscape with multiple kinetic states along the reaction pathway during the catalysis process [31], and the ligand-free *Aquifex* Adk adopts different conformations with variable degrees of the closure of lids [32]. Some of the flexible “hotspot” residues with backbone conformational alteration allowing for motif-wise lid motion, have been identified as the “hinges”, thereby raising an assumption that the amplitude of the fast internal motion of the hinges on the ps-ns timescale is mechanistically responsible for the biocatalytically significant lid motions on the μ s-ms timescale [33]. Furthermore, molecular dynamics (MD) simulation of a sextuple mutant of *Aquifex* Adk supports this assumption by characterizing the motion trajectories at an atomic resolution [33]. In this mutant, the non-conservative backbone-rigidifying prolines and π - π -stacking-inducing phenylalanines were replaced with the corresponding residues of an Adk homolog with lower NMR-derived S^2 values for hinge residues. In other words, the closure of lids might result from “individual attempts by local groups to overcome the energy barrier for the conformational transition” [33]. Due to the domain-wise structural and functional similarities between *Aquifex* Adk and *hAK1*, we, therefore, conjecture that the above analyses for *Aquifex* Adk is applicable to a high extent for *hAK1*.

Herein, we found that 12 key residues located at the binding interface of *hAK1* with ADP are important to *hAK1* catalytic activity based on their chemical shift perturbation after ADP addition and their enzymatic change after mutation. However, the nature of the mutation-induced catalytic activity loss in detail remains to be explored. A mechanism mediated by the mis-oriented Mg-ADP interaction is conceivable, but, in the meantime, binding incapability as a result of the misfold of *hAK1* is also a possibility. Expectedly, a combination of our biophysical analysis with the high-precision MD simulations might better illustrate the motional patterns of the mutants, thus facilitating the molecular mechanism underlying the catalytically relevant residues. What is more, we also found that five residues (L43, M61, L66, R128 and V182), which were located at the binding interface of *hAK1*, did not show significant chemical shift perturbations in the NMR titration experiments, suggesting that they were not greatly involved in Mg-ADP binding to *hAK1*. We, thus, speculate these residues were not closely related to the catalytic function of *hAK1*. However, mutation experiments and catalytic activity measurements are needed to perform in the future to examine whether these residues are catalytic important for *hAK1*.

This study mainly focused on biophysically clarifying the structural basis of *hAK1* catalyzing ADP into ATP and AMP, and, with the critical discussions above, it is necessary to address the atom-level revelation of the molecular mechanism describing the dynamics of *hAK1* binding the substrate. To this end, molecular docking of *hAK1* and its substrates as well as relevant molecular dynamics simulation have been included in our future plan and are actually under our investigation, which will facilitate further understanding of the molecular mechanism of *hAK1* functions.

In summary, our study is beneficial to further understanding the role of conformational fluctuations involved in the enzymatic activities of *hAK1*, and provides insights into contributions of internal motions on different timescales to conformational changes induced by Mg^{2+} -ADP binding.

Author Contributions: Conceptualization, C.G., H.Z., W.L. and D.L.; methodology, C.G., H.Z., W.L., H.C., T.C., Z.W., J.Y. and D.L.; validation, C.G., H.Z. and D.L.; formal analysis, C.G., H.Z., W.L., H.C., J.Y. and D.L.; investigation, C.G., H.Z. and D.L.; resources, C.G. and D.L.; data curation, C.G., and H.Z.; writing—original draft preparation, C.G. and H.Z.; writing—review and editing, C.G., H.Z. and D.L.; visualization, H.Z., W.L. and H.C.; supervision, C.G. and D.L.; project administration, D.L.; funding acquisition, C.G. and D.L. All authors have read and agreed to the published version of the manuscript.

Funding: This research was funded by the Natural Science Foundation of Fujian Province (No. 2020J01022).

Data Availability Statement: The solution structure of *hAK1* has been deposited in the Protein Data Bank with an accession code of 7X7S (<https://www.rcsb.org/structure/unreleased/7X7S> accessed on 10 June 2022).

Acknowledgments: The authors are grateful to Liubin Feng of the College of Chemistry and Chemical Engineering, Xiamen University for help with NMR experiments.

Conflicts of Interest: The authors declare no conflict of interest.

References

1. Downs, S.M.; Hudson, E.R.; Hardie, D.G. A Potential Role for AMP-Activated Protein Kinase in Meiotic Induction in Mouse Oocytes. *Dev. Biol.* **2002**, *245*, 200–212. [[CrossRef](#)] [[PubMed](#)]
2. Lee, J.H.; Koh, H.; Kim, M.; Kim, Y.; Lee, S.Y.; Karess, R.E.; Lee, S.-H.; Shong, M.; Kim, J.-M.; Kim, J.; et al. Energy-Dependent Regulation of Cell Structure by AMP-Activated Protein Kinase. *Nature* **2007**, *447*, 1017–1020. [[CrossRef](#)] [[PubMed](#)]
3. Brenman, J.E. AMPK/LKB1 Signaling in Epithelial Cell Polarity and Cell Division. *Cell Cycle* **2007**, *6*, 2755–2759. [[CrossRef](#)] [[PubMed](#)]
4. Zwerschke, W.; Mazurek, S.; Stöckl, P.; Hütter, E.; Eigenbrodt, E.; Jansen-Dürr, P. Metabolic Analysis of Senescent Human Fibroblasts Reveals a Role for AMP in Cellular Senescence. *Biochem. J.* **2003**, *376*, 403–411. [[CrossRef](#)]
5. Panayiotou, C.; Solaroli, N.; Karlsson, A. The Many Isoforms of Human Adenylate Kinases. *Int. J. Biochem. Cell. B* **2014**, *49*, 75–83. [[CrossRef](#)]
6. Dzeja, P.P.; Zeleznikar, R.J.; Goldberg, N.D. Adenylate Kinase: Kinetic Behavior in Intact Cells Indicates It Is Integral to Multiple Cellular Processes. *Mol. Cell. Biochem.* **1998**, *184*, 169–182. [[CrossRef](#)]
7. Shapiro, Y.E.; Meirovitch, E. Activation Energy of Catalysis-Related Domain Motion in *E. Coli* Adenylate Kinase. *J. Phys. Chem. B* **2006**, *110*, 11519–11524. [[CrossRef](#)]
8. Reinstein, J.; Vetter, I.R.; Schlichting, I.; Roesch, P.; Wittinghofer, A.; Goody, R.S. Fluorescence and NMR Investigations on the Ligand Binding Properties of Adenylate Kinases. *Biochemistry* **1990**, *29*, 7440–7450. [[CrossRef](#)]
9. Müller, C.W.; Schulz, G.E. Structure of the Complex between Adenylate Kinase from *Escherichia Coli* and the Inhibitor Ap₅A Refined at 1.9 Å Resolution: A Model for a Catalytic Transition State. *J. Mol. Biol.* **1992**, *224*, 159–177. [[CrossRef](#)]
10. Müller, C.; Schlauderer, G.; Reinstein, J.; Schulz, G. Adenylate Kinase Motions during Catalysis: An Energetic Counterweight Balancing Substrate Binding. *Structure* **1996**, *4*, 147–156. [[CrossRef](#)]
11. Pelz, B.; Žoldák, G.; Zeller, F.; Zacharias, M.; Rief, M. Subnanometre Enzyme Mechanics Probed by Single-Molecule Force Spectroscopy. *Nat. Commun.* **2016**, *7*, 10848. [[CrossRef](#)] [[PubMed](#)]
12. Miron, S.; Munier-Lehmann, H.; Craescu, C.T. Structural and Dynamic Studies on Ligand-Free Adenylate Kinase from *Mycobacterium Tuberculosis* Revealed a Closed Conformation that Can Be Related to the Reduced Catalytic Activity. *Biochemistry* **2004**, *43*, 67–77. [[CrossRef](#)]
13. Bellinzoni, M.; Haouz, A.; Graña, M.; Munier-Lehmann, H.; Shepard, W.; Alzari, P.M. The Crystal Structure of *Mycobacterium Tuberculosis* Adenylate Kinase in Complex with Two Molecules of ADP and Mg^{2+} Supports an Associative Mechanism for Phosphoryl Transfer. *Protein Sci.* **2006**, *15*, 1489–1493. [[CrossRef](#)] [[PubMed](#)]
14. Fu, C.; Peng, Y.; Liao, X.; Guo, C.; Lin, D. ¹H, ¹³C, ¹⁵N Backbone and Side-Chain Resonance Assignments of the Human Adenylate Kinase 1 in Apo Form. *Biomol. NMR Assign.* **2013**, *7*, 155–158. [[CrossRef](#)] [[PubMed](#)]
15. Rieping, W.; Habeck, M.; Bardiaux, B.; Bernard, A.; Malliavin, T.E.; Nilges, M. ARIA2: Automated NOE Assignment and Data Integration in NMR Structure Calculation. *Bioinformatics* **2007**, *23*, 381–382. [[CrossRef](#)] [[PubMed](#)]
16. Shen, Y.; Bax, A. Protein Backbone and Sidechain Torsion Angles Predicted from NMR Chemical Shifts Using Artificial Neural Networks. *J. Biomol. NMR* **2013**, *56*, 227–241. [[CrossRef](#)]

17. Laskowski, R.A.; MacArthur, M.W.; Moss, D.S.; Thornton, J.M. PROCHECK: A Program to Check the Stereochemical Quality of Protein Structures. *J. Appl. Crystallogr.* **1993**, *26*, 283–291. [[CrossRef](#)]
18. Borglund, E.; Brolin, S.E.; Ågren, A. Fluorometric Microassays of Adenylate Kinase, an Enzyme Important in Energy Metabolism. *Ups. J. Med. Sci.* **1978**, *83*, 81–84. [[CrossRef](#)]
19. Lipari, G.; Szabo, A. Model-Free Approach to the Interpretation of Nuclear Magnetic Resonance Relaxation in Macromolecules. 1. Theory and Range of Validity. *J. Am. Chem. Soc.* **1982**, *104*, 4546–4559. [[CrossRef](#)]
20. Lipari, G.; Szabo, A. Model-Free Approach to the Interpretation of Nuclear Magnetic Resonance Relaxation in Macromolecules. 2. Analysis of Experimental Results. *J. Am. Chem. Soc.* **1982**, *104*, 4559–4570. [[CrossRef](#)]
21. Dosset, P.; Hus, J.-C.; Blackledge, M.; Marion, D. Efficient Analysis of Macromolecular Rotational Diffusion from Heteronuclear Relaxation Data. *J. Biomol. NMR* **2000**, *16*, 23–28. [[CrossRef](#)] [[PubMed](#)]
22. Cole, R.; Loria, J.P. FAST-Modelfree: A Program for Rapid Automated Analysis of Solution NMR Spin-Relaxation Data. *J. Biomol. NMR* **2003**, *26*, 203–213. [[CrossRef](#)] [[PubMed](#)]
23. Farrow, N.A.; Zhang, O.; Szabo, A.; Torchia, D.A.; Kay, L.E. Spectral Density Function Mapping Using ¹⁵N Relaxation Data Exclusively. *J. Biomol. NMR* **1995**, *6*, 153–162. [[CrossRef](#)]
24. Spyropoulos, L. A Suite of Mathematica Notebooks for the Analysis of Protein Main Chain ¹⁵N NMR Relaxation Data. *J. Biomol. NMR* **2006**, *36*, 215. [[CrossRef](#)]
25. Cui, D.-C.; Ren, W.-T.; Li, W.-F.; Wang, W. Metadynamics Simulations of Mg²⁺ Transfer in the Late Stage of the Adenylate Kinase Catalytic Cycle. *Acta Phys.-Chim. Sin.* **2016**, *32*, 429–435. [[CrossRef](#)]
26. Onuk, E.; Badger, J.; Wang, Y.J.; Bardhan, J.; Chishti, Y.; Akcakaya, M.; Brooks, D.H.; Erdogmus, D.; Minh, D.D.L.; Makowski, L. Effects of Catalytic Action and Ligand Binding on Conformational Ensembles of Adenylate Kinase. *Biochemistry* **2017**, *56*, 4559–4567. [[CrossRef](#)]
27. Lescop, E.; Lu, Z.; Liu, Q.; Xu, H.; Li, G.; Xia, B.; Yan, H.; Jin, C. Dynamics of the Conformational Transitions in the Assembling of the Michaelis Complex of a Bisubstrate Enzyme: A ¹⁵N Relaxation Study of *Escherichia Coli* 6-Hydroxymethyl-7,8-Dihydropterin Pyrophosphokinase. *Biochemistry* **2009**, *48*, 302–312. [[CrossRef](#)]
28. Song, H.D.; Zhu, F. Conformational Dynamics of a Ligand-Free Adenylate Kinase. *PLoS ONE* **2013**, *8*, e68023. [[CrossRef](#)]
29. Hollingsworth, S.A.; Dror, R.O. Molecular Dynamics Simulation for All. *Neuron* **2018**, *99*, 1129–1143. [[CrossRef](#)]
30. Pawnikar, S.; Bhattarai, A.; Wang, J.; Miao, Y. Binding Analysis Using Accelerated Molecular Dynamics Simulations and Future Perspectives. *AABC* **2022**, *15*, 1–19. [[CrossRef](#)]
31. Kerns, S.J.; Agafonov, R.V.; Cho, Y.-J.; Pontiggia, F.; Otten, R.; Pachov, D.V.; Kutter, S.; Phung, L.A.; Murphy, P.N.; Thai, V.; et al. The Energy Landscape of Adenylate Kinase during Catalysis. *Nat. Struct. Mol. Biol.* **2015**, *22*, 124–131. [[CrossRef](#)] [[PubMed](#)]
32. Henzler-Wildman, K.A.; Thai, V.; Lei, M.; Ott, M.; Wolf-Watz, M.; Fenn, T.; Pozharski, E.; Wilson, M.A.; Petsko, G.A.; Karplus, M.; et al. Intrinsic Motions along an Enzymatic Reaction Trajectory. *Nature* **2007**, *450*, 838–844. [[CrossRef](#)] [[PubMed](#)]
33. Henzler-Wildman, K.A.; Lei, M.; Thai, V.; Kerns, S.J.; Karplus, M.; Kern, D. A Hierarchy of Timescales in Protein Dynamics Is Linked to Enzyme Catalysis. *Nature* **2007**, *450*, 913–916. [[CrossRef](#)] [[PubMed](#)]